Study of the spatter distribution on the powder bed during selective laser melting

Ahmad Bin Anwar[a,b], Quang-Cuong Pham[a]

[a] *Singapore Centre for 3D Printing, School of Mechanical and Aerospace Engineering, Nanyang Technological University, 50 Nanyang Ave, Singapore 639798*
[b] *SLM Solutions Singapore Pte Ltd, 25 International Business Park # 02-15/17, German Centre, Singapore 609916*

Abstract

In Selective Laser Melting (SLM), inert gas is pumped into the chamber to eliminate the deleterious by-products, which includes spatter. Despite this, traces of spatter on the powder bed have always been observed. Earlier research mainly focussed on the formation and characterization of spatter particles that were freshly ejected from the melt pool. However, in this study, the quantification of the spatter distribution on the powder bed was performed, following their transport by the inert gas flow which was varied at two gas pump settings (60 and 67 %). Image processing for spatter detection based on contrast was first conducted. The sieved out spatter particles were quantified by precision weighing of mass. Optical microscopy was then utilised for size determination. The majority of spatter particles were originally distributed along the −x direction, as observed from the top down images taken. It was found that spatter was generally transported in the −x direction with the mass and size gradually decreasing with distance from the scanned regions. However, increasing the gas flow velocity did not correspond to a lesser mass distribution. Computations on the Stk number revealed that at the gas pump setting of 67 %, spatter particles of greater size were deposited earlier on the powder bed, suggesting that increasing the gas flow velocity to a large extent would increase the likelihood of powder bed contamination. The forward extrapolation of the exponential Stk number trendlines also elucidated the reason for the limitations on the width of the powder bed in machines designed by SLM Solutions.

Keywords: Additive Manufacturing, Selective Laser Melting, Spatter Particles, Inert Gas Flow, Digital Image Processing

Email address: ahmadbin001@e.ntu.edu.sg (Ahmad Bin Anwar)

1. Introduction

The spattering phenomenon is generally observed during laser-based machining and manufacturing processes such as laser drilling, cutting, welding and also powder bed fusion systems. In such processes, spattering refers to the ejection of molten material from the melt pool, followed by solidification and then possible deposition onto nearby regions or removed by an inert gas shield. Spattering in Selective Laser Melting (SLM) has been investigated through the use of high speed imaging and modelling [1]. It was concluded that the Marangoni effects in the melt pool coupled with the recoil pressure exerted by the metal vapour expansion were mainly responsible for the eventual ejection of molten material. A three-dimensional high fidelity power-scale model which showed how the melt pool dynamics generated spattering and pores during SLM was also introduced [2]. It was also reported that recoil pressure by the gas plume ejected molten metal which were initially elongated, eventually disintegrated into smaller droplets to minimise surface energy. Alternatively, hydrodynamic analysis together with a single phase flow model was developed to show how the entrainment of micro particles by the ambient gas flow is actually responsible for the ejection of spatter as compared to the recoil pressure by metal vapour theory [3]. More recently, applied high speed imaging and schlieren imaging were applied together with multiphysics modelling to demonstrate how metallic jet vapours become entrained into the plasma plume and its interactions with the argon gas flow [4]. Notably, the simulations performed did not include transport of spatter by the gas flow leading to its eventual deposition on the powder bed.

The effects of spatter are both cosmetic and detrimental to the part's properties, which could potentially lead to part failure. For example, it was discovered that the difficult removal of overlapped spatter between holes made using laser percussion drilling, caused superficial degradation to the workpiece and also the hole geometries [5]. Thermal gradients that arise when a spatter lands on a colder region of the weld metal would act as a localized stress raiser serving as crack initiation sites [6]. Therefore, attempts have been made to minimise or completely remove the spatter. A recent study involved three methods to remove the spatter in situ during a laser ablation process of aluminium composites [7]. They include using an argon gas jet and fused silica plates with the former only proving to be efficient for 1 - 2 kW laser pulses. Nevertheless, in terms of the material, bulk metal is used as the workpiece in such laser-based manufacturing and machining processes while material powder is used in SLM.

In SLM, the powder bed layer thickness is inversely proportional to the energy density (Ψ), such that $\Psi = P/(v \cdot h \cdot t)$, where P is the laser power, v is scan velocity, h is hatch space and t is layer thickness [8]. Spattered particles were analysed using Scanning Electron Microscopy (SEM) and it was found that they were significantly larger than the starting fresh powder [9]. Thus, deposition of spatter during SLM will undoubtedly disrupt the layer thickness uniformity of the powder bed. For example, layer thickness has a significant effect on the microstructure of Al/Fe_2O_3 powder due to the amount of oxygen found in the matrix[10]. Subsequently, it was concluded that the larger spatter

particles were incompletely melted by the laser scanning, leading to the introduction of inclusions which acted as crack initiation sites during tensile testing [11, 12]. The latter also reported three different types of spatter during the SLM of CoCr alloy; metallic jet spatter, droplet spatter and unmelted powder spatter, which caused negative effects on the microstructure and properties of the printed parts. The microstructures of SLM parts were also affected by material vaporisation due to the presence of volatile elements with low boiling points leading to the introduction of undesired pores [13, 14]. Characterisation of new and recycled (contaminated) nickel alloy powder showed that the porosity levels increased while the ductility and impact toughness of the printed parts decreased [15]. Energy Dispersive X-ray Spectroscopy (EDS) micro-analysis on larger particles with oxides, affected the fatigue life of AlSi10Mg parts produced by SLM [16]. Re-depositions of process by-products in regions of low flow velocity in SLM (near the gas outlet) has also been recorded [17]. Beam scattering was also suggested to have occurred near such regions, causing larger scan vector widths than that of the input. More recently, high speed photography and image analysis were used to investigate the formation mechanism and distribution of induced spatter [18]. Andani et al. [19] also showed that increasing the laser speed or decreasing the power reduced the amount of spatter generated. The amount and sizes of spatter that were immediately expelled from the melt pool, were quantified and reported following image processing of data from high speed camera recordings. Spatter was also seen to be deposited on solidified melt pools. Their quantification study on focussed on spatter which newly ejected spatter from the melt pool and suspended above the powder bed, as well as powder analysis before and after the SLM process. More importantly, the role of the inert gas flow in transporting the spatter and influencing the spatter distribution on the powder bed were not reported. The detailed powder bed spatter distribution could be crucial when one is placing multiple part files on the substrate prior to the start of the build job.

In terms of spattering, much research has been dedicated to investigating their formation and effects, via both experiments and simulations. However, limited study has been done on characterising spatter ejection in three-dimensions with the use of two high speed cameras [3, 4]. More noticeably, simulations of spatter transport by the gas flow have not yet been performed other than the simulation studies done by Philo et al. [20] which showed that spatter accumulation on the powder bed decreased by 26.64 % through modifications on the gas inlet design for the Renishaw AM250 machine. Nonetheless, the scanning strategy or laser parameters were not mentioned in their experimental work on SLM of stainless steel 316L.

In our earlier studies, it was found that laser scanning against the inert gas flow led to a greater accumulation of spatter in the region outside the powder bed and close to the gas outlet [21]. Following that, the effects of varying scan direction, part placement and also gas flow velocity on the Ultimate Tensile Strength (UTS) were then statistically studied using the Analysis of Variance (ANOVA) method [22]. With the use of a high-speed camera, laser-spatter interactions were recorded and analysed. It was proven that when scanning in

the direction of the gas flow, spatter was more likely to be transported into the beam path. Consequently, heat energy from the laser was wasted in burning such spatter leading to the incomplete melting and therefore increased porosity levels of the printed parts which inevitably had lower UTS.

To the best of our knowledge, no research has been conducted on the spatter distribution on the powder bed under the influence of the inert gas flow due to unidirectional scanning for the SLM of aluminium alloy powder, AlSi10Mg. Such data would be able to serve as the ground truth for the mentioned simulation studies. Thus, in this work, we performed the quantification of spatter distribution on the powder bed by using image processing, followed by direct mass measurements with precision weighing and finally size measurements using optical microscopy.

2. Related work

Studies have been made to characterize the deposited spatter on the workpiece in welding and laser drilling. For example, a spatter index was introduced to quantify the spatter in welding using computer vision which was reported to be highly reliable [23]. The authors also concluded that using incandescent light at low angles to the workpiece served as the best arrangement for illumination. Human perception and physical dimension measurements were also employed in the study. Characterisation of the spatter deposition area using image acquisition, processing and analysis was carried out by varying the laser processing parameters in laser percussion drilling [24]. No quantitative measurements of the amount and dimensions of spatter were performed in the study. An X-ray transmission system was also developed for characterizing spatter in wet welding where the largest spatter was measured at approximately 4.5 mm [25] . In the case of powder bed fusion processes, a review of the available powder characterisation methods and the effects of varying powder characteristics on part properties was conducted [26, 27]. The techniques include sieve analysis, microscopy (to obtain high resolution images) and also laser diffraction, each with their own pros and cons. However, their work evaluated the fresh powder used for part fabrication and notably excluded any investigations on spatter and other by products. Spatter distribution on the workpiece was also not investigated.

Regarding the image processing of powder, limited research has been performed on material powder commonly used in Additive Manufacturing (AM). Most recently, image texturing using the bag of visual words computer vision method could supplement existing powder characterisation techniques for AM [28]. Their research only accounted for the fresh powder feedstock in AM and not specifically spatter-contaminated powder. In another study, an in-situ analysis of spatter as a process signature driver was employed to indicate under or over-melting conditions during SLM [29]. In other applications, pharmaceutical powder was analysed using a multivariate gray image analysis and it was found that the results were comparable to that using near-infrared spectroscopy [30].

Subsequently, implementation of an algorithm based on the invariant image moments was used to characterise pharmaceutical powder according to morphology and size, despite contact between the particles [31]. Powder particle size was also measured with digital image processing, specifically Matlab [32]. However, the images were taken using SEM, which while useful when obtaining the particles sizes, it is impractical if one intends to investigate the in-situ spatter distribution on the powder bed immediately.

3. Materials and Methods

As mentioned earlier, three types of spatter had been reported [12]. Since droplet spatter generally gets ejected from the rear of the melt pool when laser scanning at higher speeds, maximum amount of spatter would get deposited on the powder bed by the gas flow when scanning against it. Therefore, in this work, unidirectional scanning was adopted in the +x direction to allow more spatter to be collected for quantification purposes.

In order to evaluate the effectiveness of the gas flow in transporting the spatter away from the laser-scanned regions to the chamber outlet, only the gas flow velocity is varied, which is controlled by the gas pump setting prior to the build job initialisation. It was set to 60 and 67 %, which are the lower and upper limits of the range for gas pump setting as indicated in the SLM 280 HL machine user manual. The main reason is that should the pump setting be lower than 60 %, spatter will not be effectively removed from the powder bed, leading to undesired contamination and possible protrusion into the following powder layer. On the other hand, when the pump setting is greater than 67 %, there would be a high possibility of fresh powder getting picked up by the gas flow. Consequently, the powder layer uniformity would be disrupted and inter-layer bonding would be weakened.

3.1. SLM Parameters

The SLM Solutions 280 HL (SLM Solutions Group AG, Lübeck, Germany) machine equipped with a twin (2 x 400 W) CW Ytterbium fibre laser was used in the experiments. The power bed has a dimension 280 $\times$ 280 mm. The laser beams had a focal point diameter of approximately 80 μm. Prior to the experiments, the build chamber was flooded with argon gas to reduce the oxygen level to less than 0.1%, and the flow was maintained throughout the experiment. The gas was blown from the right side of the build chamber towards the left. The build platform was pre-set to a temperature of 150°C before laser initialization. Other parameters set in the SLM Build Processor include: laser power of 350 W, layer thickness of 100 μm, laser speed of 900 mm/s and hatch space of 0.12 mm.

Spherical AlSi10Mg which had been gas atomised with nitrogen was used as printing powder. A Scanning Electron Microscope (SEM) image of the fresh powder is seen in Fig. 1. The particle size distribution is 20 - 63 μm, while the chemical composition is listed in Table 1. The chemical composition was obtained from the powder supplier, SLM Solutions.

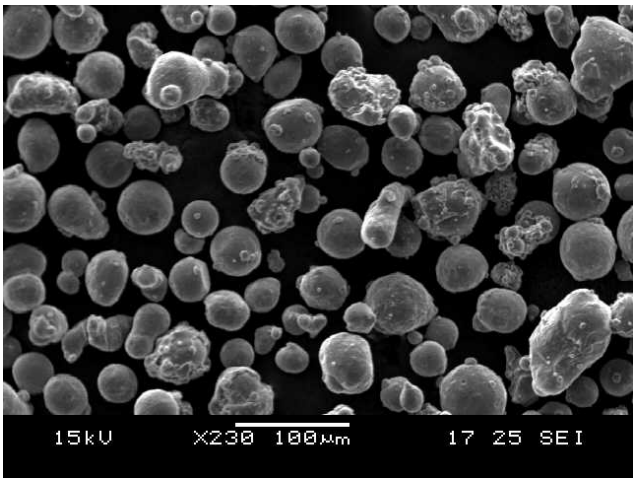

Figure 1: SEM image of fresh AlSi10Mg powder

Table 1: Chemical composition (weight %) of AlSi10Mg

Element	**Minimum**	**Maximum**
Al	Balance	Balance
Si	9.000	11.000
Fe	0.250	0.450
Mg	-	0.400
Cu	-	0.050
Zn	-	0.100
Ti	-	0.150
Mn	-	0.005
Ni	-	0.050

3.2. Gas Flow

Gas flow velocity was measured using hot wire anemometry for accurate readings with good spatial resolution and high frequency response. Measurement points were selected to be at 3 points regularly spaced apart, for both the top and bottom gas inlet. The measurements only started when the gas pump was allowed to be switched on, i.e. when the oxygen level inside the chamber was below 2%.

At 60 and 67 % of maximum gas pump input, the recorded velocity was at 1.41 ± 0.24 m/s and 1.57 ± 0.21 m/s at the bottom gas rail inlet respectively. It should be noted that the actual gas velocity at the inlets fluctuate according to the condition of the gas filter. Overtime, for the same gas pump setting, the actual velocity output decreases due to waste build up at the filter since the argon gas is recirculated back into the chamber by the pump. Therefore, the

experiment sets were conducted continuously to ensure that the filter status was relatively maintained at 43.5 ± 0.3 mbar during the SLM process.

3.3. Experiment protocol

To study the spatter distribution closely, the powder bed was segmented into equal sized columns of 40 × 120 mm as seen in Fig. 2. Images of the powder bed directly after laser scanning was performed first, in order to obtain an initial overview of the untouched powder bed and possible disruptions caused by the motion of the recoater. Characterisation of the spatter distribution on the powder bed was done by mass measurement and then size determination. The spatter was collected after 20 laser-scanned layers to ensure sufficient spatter was available for analysis. The experiment was repeated four times at 60 and 67% gas pump settings, giving a total of eight data sets.

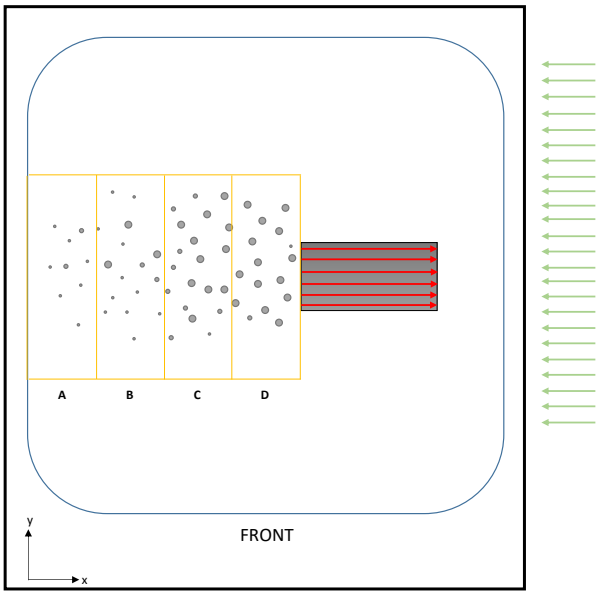

Figure 2: Layout of scanning region of 40 × 80 mm, with spatter on powder bed distributed on equal columns of 40 ×120 mm each. Red arrows resemble unidirectional laser scan vectors while green arrows represent inert gas flow. The scanning order was set from the top going downwards (-y direction)

3.3.1. Image processing

The objective is to implement a simple yet effective method of acquiring the images for analysis. Top-down images were taken using a Sony alpha a6000 camera, which has a maximum resolution of 6000 x 4000 pixels, mounted on an aluminium frame as seen in the set-up in Fig. 3 and subsequently processed using the image processing software, ImageJ. The calibration factor was determined to be 15.9 pix/mm. Lighting was provided by the built-in LED lights which lined the ceiling of the chamber closer to the front door.

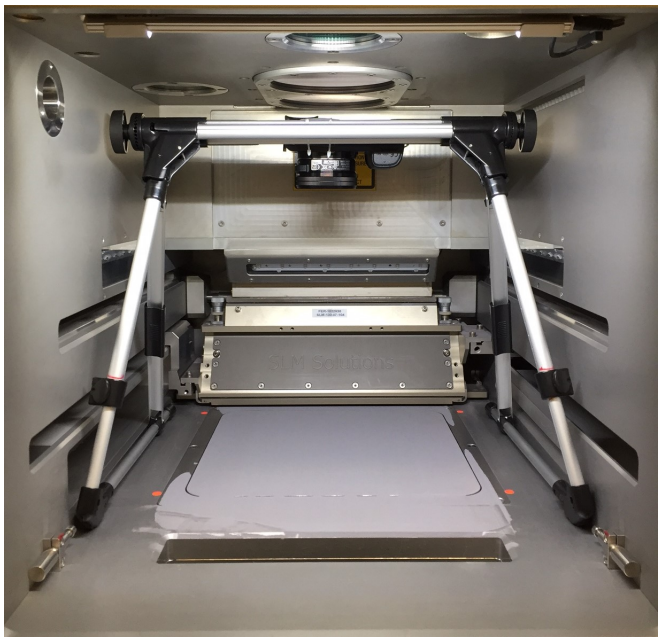

Figure 3: Image capturing set-up

To maintain consistency of the images captured, four circular neon coloured markers at 8 mm in diameter were placed outside the substrate, on the base of the chamber. The pixel coordinates of the center of each circle were determined to be used as reference points. Perspective transformation was then carried out followed by acquiring the difference between the before and after laser scanned images.

From the findings of previous studies, the sizes of spatter exceed the layer thickness used in the current study (i.e. larger than 100 μm) [9, 22]. Therefore, spatter deposited on the current layer could protrude into the subsequent layer above. However, pressure exerted during the laying of the powder by the recoater could also depress the spatter downwards, minimising any spatter protrusion.

To quantify the observed spatter, comparisons between before and after images of the laser scanned powder bed for the third to tenth layers were made, giving a total of nine pairs of images. It is important to note that since the first layer of powder is coated manually and verified by the naked eye, it is deemed not suitable for analysis due to the inevitable associated inconsistencies. Also to account for the possible unevenness of the substrate surface due to previous warpage and distortion, the third layer was identified to be suitable as the initial layer. The Renyi entropy threshold method was deemed suitable for the purpose of this study. For this method, the image was analysed globally such that a threshold was chosen from the gray level histogram based on the entropy concept derived from information theory [33].

From visual inspection of the powder bed with the naked eye, spatter particles are easily distinguishable from the fresh powder due to their darker contrast. This is reflected in the images taken using the camera. Therefore, the object of interest is distinct from the background, deeming it feasible for the image to be segmented into an object and a background. Such bilevel thresholding results in the gray level image to be bimodal. Subsequently, the selected threshold chosen corresponds to the valley of the gray level histogram. Pixels on either side of the threshold would be assigned to the background or object accordingly [34].

Spatter percentage or "SP" is then used as the term to report the quantity of pixels which approximately represents the spatter is then reported as a fraction of the individual columns (424×1272 pixels each).

3.3.2. Mass measurement

The spatter together with the fresh powder in the respective cells was collected using a handheld suction based powder collection device (BioTX Automation Inc., Livingston, Texas, U.S.A) and a regular scoop. They were then sieved one batch at a time using a mechanical shaker by Ro-Tap ®Sieve Shakers (W.S. Tyler, Ohio, USA) and a 12 inch diameter sieve with 63 μm openings as per ASTM E-11 standard. As mentioned earlier, the fresh powder used had a maximum diameter of 63 μm. From observations, the spatter particles that were sieved out appeared darker in contrast to the fresh powder and this was the case after sieving was completed.

3.3.3. Size analysis

Static image analysis was used to measure the sizes of the spatter. Therefore, the minimum size is expected to be greater than 63 μm. ImageJ software, which is an open source image processing program usually used for analysing scientific complex images, was then used to obtain the spatter diameter from the magnified images taken via optical microscopy. The spatter diameter was then reported in terms of their mean values as indicated in the standard guide for powder particle size analysis (ASTM E2651-13, Section 18.4).

Samples of collected spatter was then analysed using SEM which makes use of electrons in a vacuum environment to capture high magnification images and conduct non-destructive elemental testing on the samples. A thin layer of platinum was coated onto the spatter and the SEM images and the corresponding chemical composition was obtained using the Schottky Field Emission SEM, JSM-5600 machine (JEOL Ltd., Tokyo, Japan).

4. Results

4.1. Image processing

The typical images captured that were processed are as shown in Fig. 4. Renyi entropy thresholding method was then applied, where a dark background and white foreground which approximately represented the spatter was achieved. The resulting percentage of spatter pixels per column or Spatter Percentage (SP)

value was then determined. From Fig. 4d, it can be observed that the spatter distribution is more significant along the x direction with minor orthogonal scattering. The amount of spatter detected is seen to decrease with the distance transported in the $-$x direction. Spatter particles were also detected above and below the scanned regions.

(a)

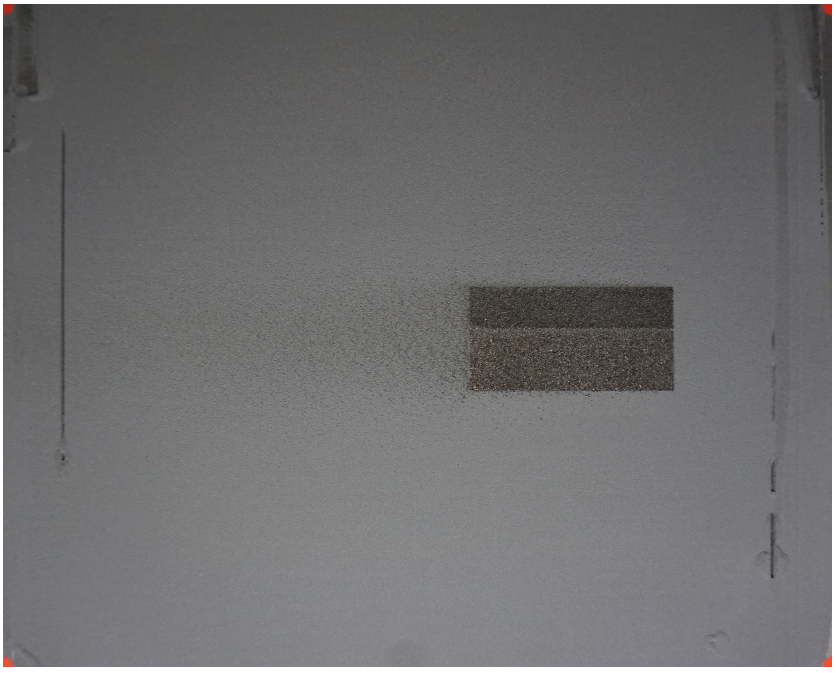

(b)

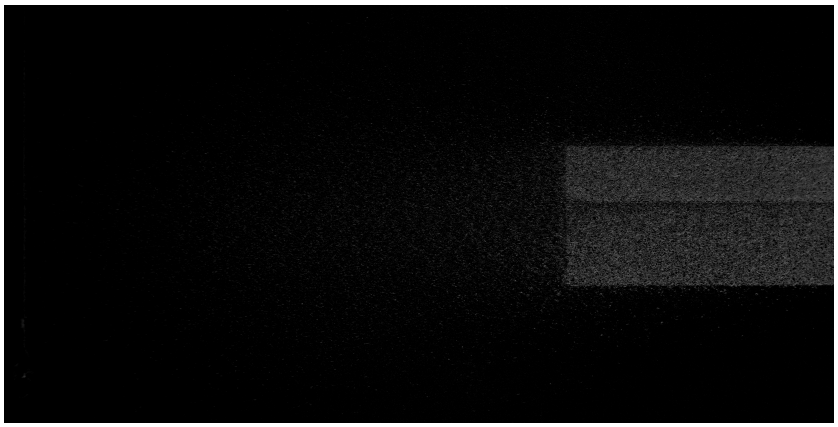

(c)

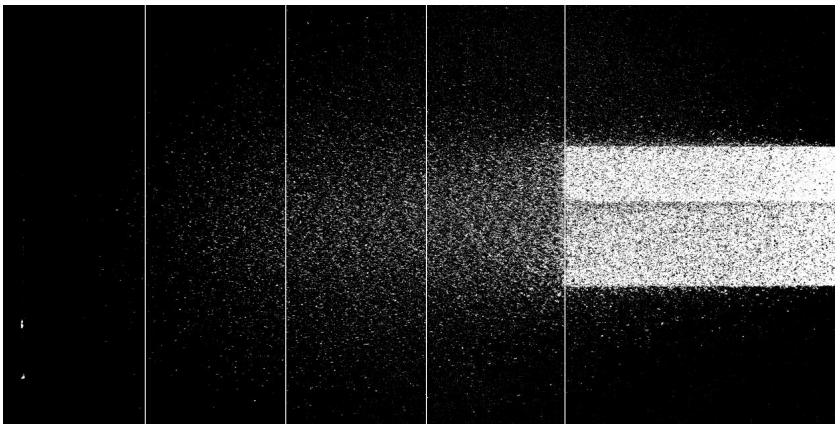

(d)

Figure 4: Typical images obtained at the tenth layer: (a) before and (b) after laser scanning (post perspective transformation), (c) result of absolute difference between image (a) and (b), (d) after application of Renyi entropy thresholding. Figures (c) and (d) have a resolution of 1272 $\times$ 2544 pixels.

4.1.1. SP of individual layers

To investigate the effect of number of layers on the SP, Fig. 5 was plotted. For both plots, it can be seen that there is a clear increase in SP with the number of layers. This is especially evident for column D at the 67 % gas pump setting, by as much as as 77.0 % from the third to the tenth layer. However for column C, the SP remains relatively constant. Columns A and B also showed relatively lower changes in SP as the number of layers increased.

From Fig. 5, the standard deviation values are seen to generally decrease for all columns with the number of powder layers. An example would be for the gas pump setting of 67 % and at column A where the standard deviation value decreased from 5.30 % for the third to 2.99 % for the tenth layer. Also the plots seem to be approaching a steady state where the fluctuations in the mean values and also standard deviation diminish with the number of layers. As such, the SP values for layer number 10 was chosen to be evaluated in this study.

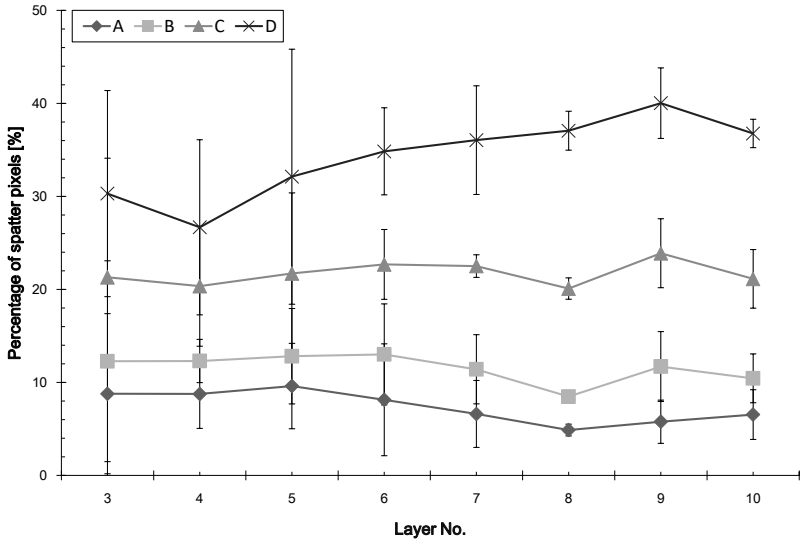

(a)

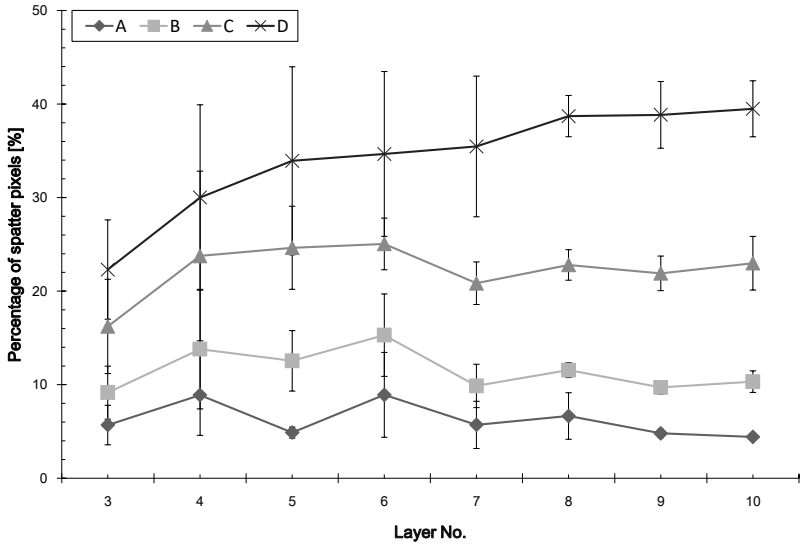

(b)

Figure 5: Plot of mean SP and standard deviation at different layer numbers for gas pump setting (a) 60 % and (b) 67 %.

4.1.2. Effect of gas flow velocity on SP

To illustrate the effect of the gas flow velocity, Fig. 6 was plotted. SP values are seen to be gradually decreasing from column D to A. For columns C and D, SP values were greater at higher gas pump setting by as much as 7.40 % for the latter. However, lesser spatter was detected for column A at this gas flow velocity with column B showing similar SP values. Thus, increasing the gas flow velocity does not correspond to a lower amount of spatter detected by the camera.

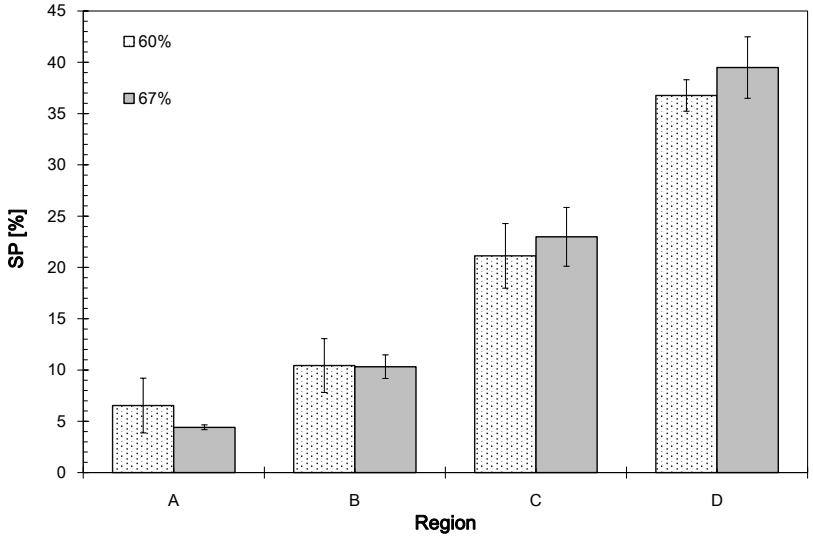

Figure 6: Bar chart of mean of summed up pixels and standard deviation representing spatter particles for each column from A to D for the tenth layer.

The illustration of the bar chart from Fig. 6 serves to provide consistency in the reporting of data together with the mass and size distributions as seen in Fig. 8 and 9. The main reason being that the spatter was collected and analysed in batches of powder collected from each segmented column. Nonetheless, to gain a better understanding of the processed images as a function of x, Fig. 7 was plotted. Each column was refined to 100 pixels in width. SP values are seen to be gradually decreasing away from the scanned region. There is also no significant difference between the SP for both gas pump setting values since the standard deviation error bars overlap. However, at the higher gas flow velocity, it is shown that slightly higher SP is recorded along the x axis.

4.2. Distribution of spatter mass on powder bed

To illustrate the effect of the gas flow velocity on mass of spatter, the spatter collected in each column was calculated and the mean was plotted as seen in Fig. 8. There is a general decrease from column D to A for both cases. However, this trend is more distinct at the higher gas pump setting. It can be clearly seen

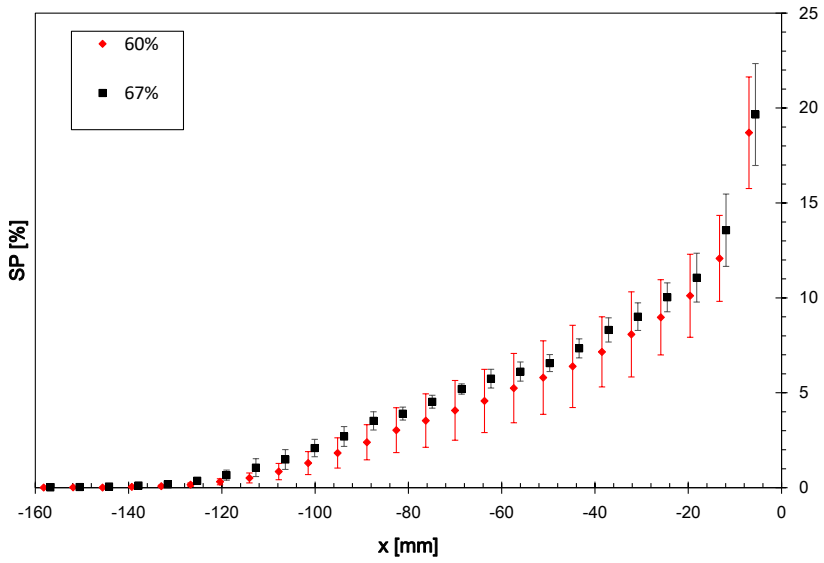

Figure 7: Plot of mean of summed up pixels and standard deviation representing spatter particles for columns of 100 pixels width or 6.29 mm. The edge of the scanned region corresponds to $x = 0$ mark.

that increasing the gas flow velocity led to the highest increase in mass values by as much as 25.5 % in column C. For column D, mass was slightly greater by 3.63 % at the lower gas pump setting. However, the effect of increasing the gas flow velocity has led to an increase in mass of spatter distribution. Further analysis is provided in the discussion section.

4.3. Distribution of spatter particle size on powder bed

The mean diameters are reported in the form of bar charts in Fig. 9. The largest particles were deposited closest to the scanned regions with values of 143.1 $\pm$ 22.6 μm and 155.9 $\pm$ 27.5 μm at 60 an 67 % gas pump settings respectively. Also, the decrease is more gradual at the lower gas pump setting. The increase in gas pump setting has led to the deposition of spatter particles with larger diameters downstream of the flow, which could explain the proportional relationship with the mass distribution as seen in Fig. 8.

4.4. Correlation between spatter mass and percentage of spatter pixels (SP)

To evaluate the effectiveness of the image processing of the powder in identifying the spatter, data from the third layer was analysed and compared against the masses of the spatter which served as the ground truth. In Fig. 10 below, the dependent variable or response is the SP while the independent variable is the mass of the spatter.

To establish their relationship quantitatively, the correlation coefficient (R) for regression was obtained. The data from the third layer was plotted, giving

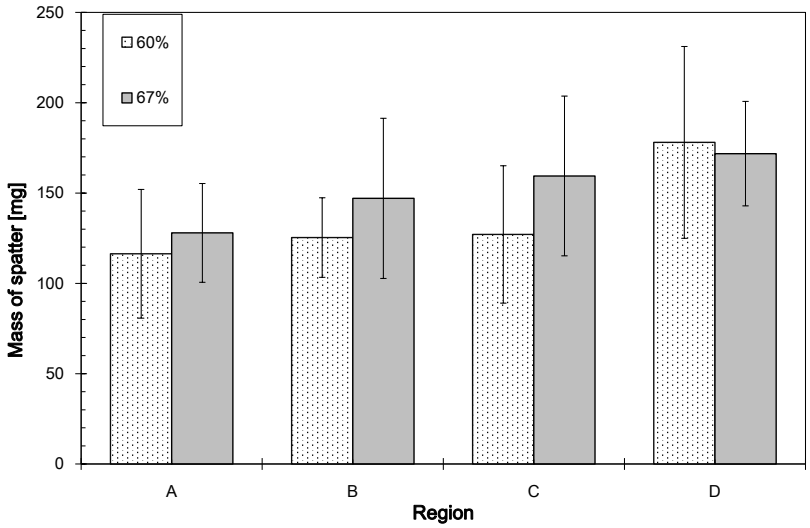

Figure 8: Bar chart of mean of summed up mass and standard deviation for each column from A to D.

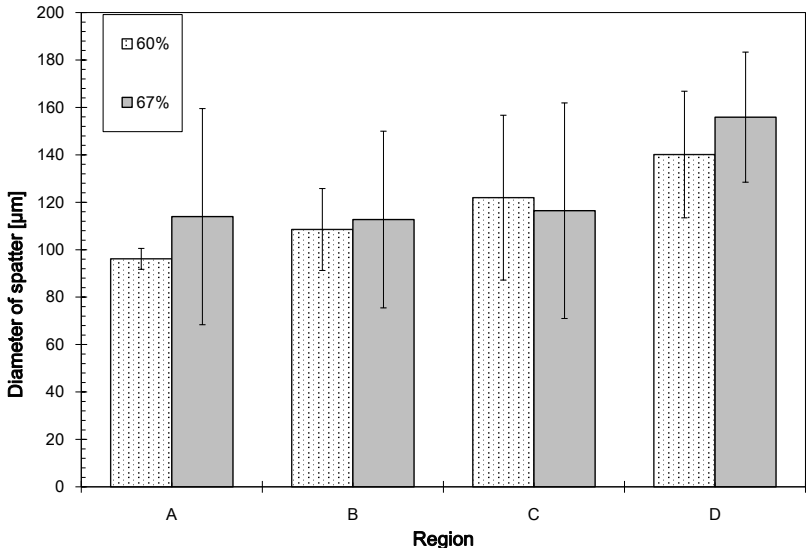

Figure 9: Bar chart of mean diameter and standard deviation for each column from A to D.

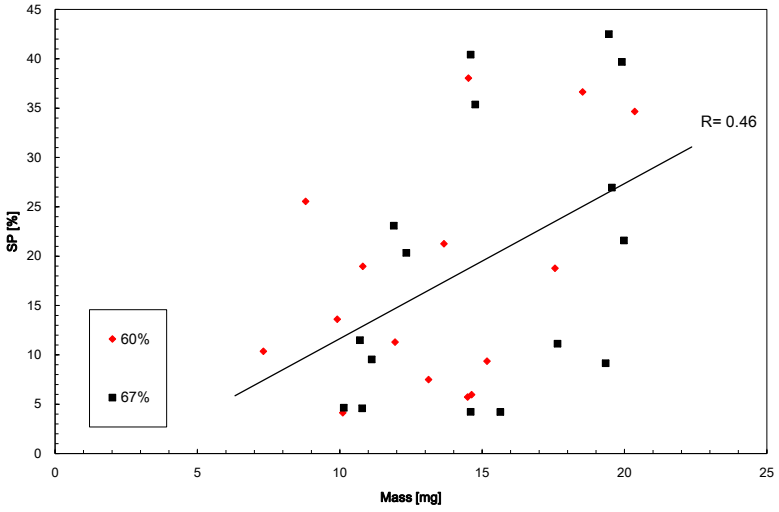

Figure 10: Plot of percentage of spatter pixels against mass of spatter for regions D to A.

a R value of 0.46 which shows that there is a moderately positive linear relationship between SP and the masses of spatter. As such, the images captured and processed are deemed to be acceptable in predicting the amount of spatter deposited on the powder bed.

It should be noted that the resolution of the images obtained using the camera were deemed not suitable for a similar plot for spatter size and SP due to the significant difference in scale between the spatter particles and that of the images.

4.5. Statistical tests

To statistically evaluate the effectiveness of the argon gas flow in transporting the spatter in the -x direction, the mean masses, sizes of spatter and SP from column A to D were subjected to two-sample t-tests with a Type 1 error probability $\alpha = 0.05$ with the number of observations, $n = 4$. The images used for SP determination in the t-tests were obtained from that of the third layer. The third layer was identified to be the first layer where the spatter could be generally observed and was minimally affected by protruding spatter from the previous layer, especially for cell D2 as seen in Fig. 5. The results of the t-tests are found in Table 2 below.

It can be seen that since the p-value for every case is greater than 0.05, the values quantified when the gas pump was set to 60 % and 67 % are not statistically significant in terms of their difference. Therefore, while increasing the gas pump setting led to a general increase in the mean values, it did not contribute to a significant increase in the distance of spatter transported.

Table 2: Statistical table for t-tests

Spatter Property	**Gas pump**	**60 %**		**67 %**		
	Column	**Mean**	**Variance**	**Mean**	**Variance**	**p-value**
Mass [mg]	A	116.4	1.3	127.9	0.7	0.313
	B	125.4	0.5	147.1	2.0	0.207
	C	127.1	1.4	159.5	2.0	0.155
	D	178.0	0.9	171.8	0.8	0.396
Diameter [μm]	A	96.1	19.4	113.9	2077.2	0.247
	B	108.5	298.4	112.7	1389.2	0.422
	C	122.0	1207.7	116.4	2064.7	0.426
	D	140.1	713.3	155.9	752.5	0.240
Percentage [%]	A	6.5	7.1	4.4	0.1	0.106
	B	10.4	6.9	10.3	1.3	0.471
	C	21.1	9.9	23.0	8.2	0.208
	D	36.4	2.9	39.5	9.0	0.090

5. Discussion

5.1. Effectiveness of image processing

To establish the effectiveness of the image processing methodology, the correlation coefficient between SP and spatter mass, was plotted as seen in Fig. 10, with an R value of 0.46. The reason for illustrating the correlation between SP and spatter mass is that mass is a collective property of the spatter, which is similar to the number of pixels representing spatter. On the other hand, the spatter sizes were reported as mean diameter values of the sampled individual spatter particles within each column obtained via optical microscopy. The high variance in terms of the spatter diameter also showed that improvements could be made in reporting the sizes of the spatter. One way to utilize the spatter size in order to reflect a better correlation with the SP would be to obtain the percentage surface area of spatter. This would require in-situ micro images of all the spatter particles following their deposition on the powder bed. However, due to the limitation inherent in the camera used during the experiments, such data acquisition proved to be unattainable. The same explanation could be applied with regards to the number of spatter particles, since it is nearly impossible to count them individually. Thus, mass of spatter served as a better variable in providing a more reliable ground truth property.

The correlation coefficient of 0.46, means that there was a clear positive correlation between the collected spatter mass and SP. This established our image processing method as an effective quantitative method to study the amount of spatter without disturbing the powder bed. We noted however that the correlation was not overwhelming. Despite this, a crucial limitation during the spatter collection is the possibility of spatter particles with diameters smaller than 63 μm not being sieved out which could possibly explain the low R value of 0.46. From a study conducted by Wang et al. [12], three types of spatter have been identified. In our study, droplet spatter was mainly analysed, due to their sizes being greater than the fresh powder, making it practical to be collected. However, the remaining two types of spatter; metallic jet and powder spatter was possibly deposited on the powder bed. Their work is supported by that of Ly et al. [3] where it was reported that three different types of spatter ejections had been recorded from high speed cameras. The sizes of such uncollected particles could have been smaller that 63 μm since it was reported that a droplet of diameter 8 μm was ejected at approximately 18 m/s.

It has been shown that visually, there is a general decrease in the amount of spatter in the $-$x direction. The reason for the detectability of the spatter by the naked eye is due to the stark difference in contrast of spatter to fresh powder. Spatter particles appeared larger and darker due to the formation of surface oxides. This difference in contrast proved to be crucial in the image processing which detected the spatter following the application of the Renyi entropy thresholding method. However, due to the larger mean diameter of the spatter as seen in Fig. 9, as compared to the input layer thickness of the powder bed (100 μm), the images taken could have revealed protruding spatter that had been deposited on previous layers. This could validate the increase

in SP for column D as seen in Fig. 5 since the diameter of spatters were the largest. On the same layer studied, overlap of spatter particles was also observed and thus the underlying spatter were not captured by the camera. Therefore, such inaccuracies along with the cumulative effect of spatter protrusion from previous layers could potentially decrease the reliability of the image processing technique. Additionally, improved lighting conditions where the illumination gradient is regular, to minimise shadows and misclassification of spatter on the powder bed is critical to obtain a more optimal bi-level image [35, 36].

Lastly, from Fig. 7, it was shown that unlike the quantification of mass and size of spatter where the particles had to be collected and sieved, image processing allows the user to analyse spatter at smaller and specific positions on the powder bed. With a higher resolution camera, even narrower regions as compared to the 100 pixel width used in Fig. 7 could be applied. This would allow optimal placement of parts on the powder bed in order to minimise contamination during SLM. The above discussion also hints that image analysis, besides offering the advantage of being an easy to set up and in-situ non-destructive method, could potentially be the most accurate method to quantify spatter distribution. However, this possibility must be further tested in future research, using other independent methods to quantify the spatter distribution.

5.2. Transport of spatter by argon gas flow

5.2.1. Validation with Stokes number

The transport of spatter by argon gas flow is essentially a form of gas-solid flow, specifically where the particle dynamics differ from that of the fluid. This is due to the particle inertia which could possibly cause selective concentration, cluster and separation [37, 38]. To verify the distribution of spatter downstream of the gas flow, the Stokes number (Stk) is used. The Stk number is a dimensionless number which characterises suspended particle behaviour in the fluid, in this case argon gas. It is defined as the ratio of the characteristic particle time to that of the flow: $Stk = {\rho_p d_p^2 U}/{18\mu_f L_0}$, where ρ_p is the particle density, d_p is the particle diameter, μ_f is the fluid dynamic viscosity and L_o is the characteristic length. As a guideline, for very fine particles which satisfy $Stk << 1$, the particle follows fluid streamlines, in other words, perfect advection or pure suspension [39]. Otherwise, for $Stk >> 1$, the particle is dominated by inertia and continues along its initial trajectory where possible particle-wall and particle-particle collisions occur[40].

Previous studies showed that surface oxides formed on the spatter due to the oxidation of the most volatile elements in the alloy were only several μm thick [9]. In this work, the density of the spatter was determined based on the assumption that the surface oxides were relatively negligible as compared to the bulk of the particle. As such, the value of ρ was taken to be 2700 kg/m^3, which is equivalent to that of the fresh powder. For the other parameters, U was found to be 1.41 and 1.57 m/s for gas pump settings 60 and 67 % respectively, $\mu_f = 2.23 \times 10^{-5}$ kg/(ms) and L_0 varied from 40 to 160 mm.

The computational results of the Stk number plotted in Fig. 11 shows an exponential relationship established where the standard errors of non-linear

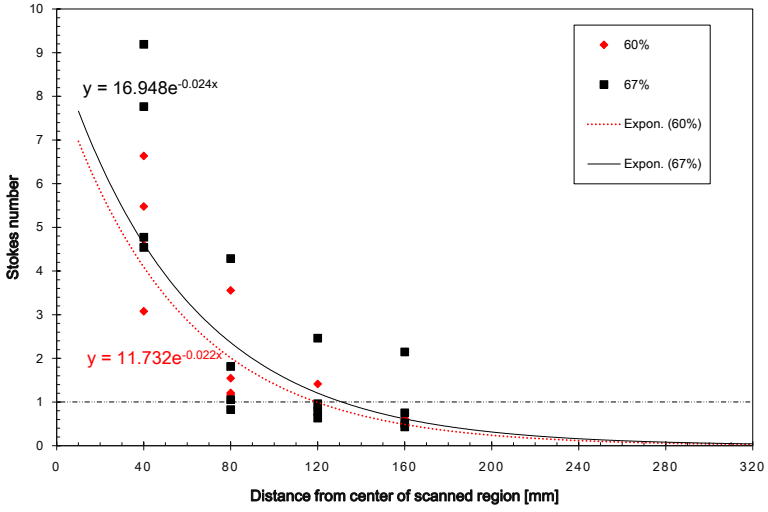

Figure 11: Plot of percentage of Stokes number for regions D to A. The characteristic length L_0 is taken from the center of the scanned region.

regression (S) obtained were 0.90 and 1.46 at the 60 and 67 % gas pump settings respectively. The Stk ranges from 0.43 to as high as 9.19. Particles with Stk greater than 1 are seen to travel not further than approximately 120 mm from the scanned region at the lower gas velocity. At the 67 % gas pump setting, this distance also increased to 130 mm, representing a 8.33 % increase in spatter transport distance. Thus, it can be seen that this range does not reveal a clear cut explanation on the nature of the spatter transport by the gas flow. Indeed, a combination of both the effect of spatter transport and the particle inertia during the particle laden flow could have most likely taken place. However, since the diameter of spatter is a function of Stk, it shows that the distribution of spatter is influenced by its size. For spatter with Stokes number lower than 1, the effect of the gas flow would dominate the particle inertia and therefore such smaller particles would be transported further downstream from column D to A, as seen in Fig. 9 [41].

For larger particles, generally there would be a correspondingly higher Stk value. By assuming that the density is independent of other variables, their mass would then have a positive linear relationship with the size of the spatter. As such, these particles would settle out of the gas flow earlier, since the high inertia which is directly proportional to its mass as related by Newton's first law, would overcome the effects of the gas flow. Additionally, gravitational forces would act to a greater extent of the heavier particles, causing them to get deposited closer to the scanned sites. Another explanation could also be that for the same magnitude of recoil pressure, the larger molten droplets would be

ejected at a lower initial momentum compared to their smaller counterparts, hence lower initial velocities would not allow such heavier spatter particles to penetrate the crossflow deep enough to be transported far before being deposited on the powder bed.

It can be seen from Fig. 11 that at 67 % gas pump setting the exponential plot is always higher. This corresponds to the relationship between the gas flow velocity on spatter detected from the images in Fig. 7 and also on the mass and size distributions in Fig. 8 and 9 respectively. With this, we can deduce that in general, the larger spatter with correspondingly larger Stk did not effectively follow the inert gas flow in the $-$x direction. Possibly, a larger fraction of spatter did not deposit near the main central region of accumulation but instead would scatter along their own respective trajectories. As a result, such anomalous spatter particles were not detected successfully by the camera leading to the low R value of 0.46. Thus, further developments in terms of accurately capturing the spatter particles by using a more advanced lens or camera is critical in order to effectively assess the spatter distribution visually.

Wall surface roughness introduced by the presence of the powder bed also induces velocity fluctuations on the crossflow. It was shown that in the case of particle laden flow, the streamwise component of the particle r.m.s velocities did not differ significantly, for the case of 60 and 130 μm particles [40]. Due to the saltation effect coupled with the wall surface roughness, particles travelling upwards have a smaller horizontal velocity as compared to downward moving particles. This is due to the latter being accelerated by the fluid flow. In their work, it was also reported that the particle velocity fluctuations could have been affected by their size distribution since smaller particles experienced lower fluctuations. Additionally, Sommerfeld and Kussin [42] reported that increasing wall roughness is significantly affects the transport velocity of particles where their fluctuating energy is intensified. Due to the particle collision with the wall and in this case the powder bed, rotational effects could also take place, imposing the Magnus lift force, as studied by Hussainov et al. [43].

Interestingly, when the linear plots from Fig. 11 are extrapolated, the exponential curves converges approximately at the 320 mm mark. Thus the region where the Stk value reaches zero, which is the case where the particles follow the gas flow streamlines completely, would be near the edge of the powder bed or substrate. This coincides critically with the limitations inherent in all variants SLM Solutions Group AG's machines, where the powder bed has been restricted to 280 mm for the x dimension due to the overall effectiveness of the gas flow in transporting spatter away from the powder bed [44]. In other words, should a spatter particle with Stk value of 0 begin its transport by the inert gas flow at the edge closest to the gas inlet, the furthest distance it would theoretically cover is 280 mm, as suggested by the exponential plots in Fig. 11.

5.2.2. Spatter ejection profiles

Prior to being transported by the inert gas flow, the spatter gets ejected from the melt pool due to the coupling effects of recoil pressure and Marangoni convection within the melt pool [1, 2]. The ejection profiles have been qualitatively

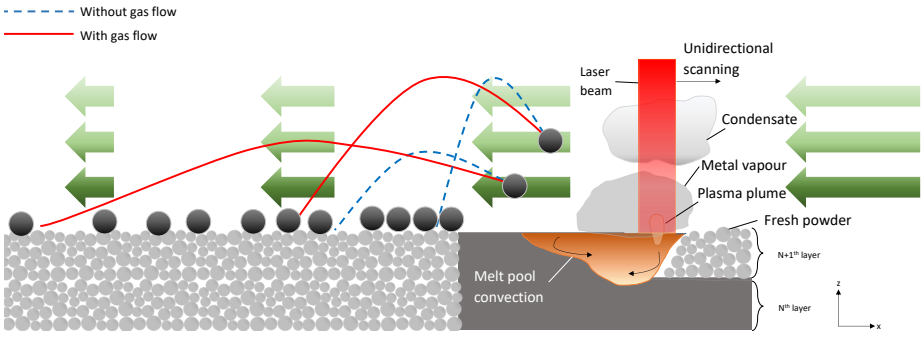

Figure 12: Schematic of spatter ejection profiles from melt pool and the effect of gas flow in the particle trajectories.

reported in earlier studies where high speed cameras were used to capture the images [3, 12, 4]. It can be seen that when the laser scanning speed increases, the ejection profiles would generally shift from vertically upwards (90°) to a relatively smaller angle to the powder bed [3]. Also, the images were taken in a two dimensional plane (x-z) and information on whether spatter was ejected in the y direction was not reported. Such information that has not been recorded could determine the deposition of spatter on the powder bed.

The reason the ejection profiles, specifically in terms of the angle and velocity, are critical in the distribution of spatter is that their inertia at the initial ejection could prove to be influential in the eventual deposition locations. Fig. 12 shows how the trajectories of the particles would extend from the presence of the gas flow. For example, for the same particles mass and size, those that ejected at high velocities and large angles would have high kinetic energies which translates to a higher trajectory in the absence of gas flow. On the other hand, those ejected at lower angles would not get deposited far from the scanning sites. Bidare et al. [4] observed that the ejected particles possessed sufficient upwards momentum to not be subjected to the crossflow in the initial phase of their trajectories. However, gravitational forces would bring them back down and eventually be carried by the inert gas crossflow. Regardless, in SLM, the presence of the gas flow would transport these particles in the further downstream in the $-$x direction, and therefore their distribution would depend more heavily on the Stokes number as explained earlier.

A full study of the effects of the inert gas crossflow, laser power and speed on the spatter distribution is beyond the scope of the current study, hence the lack of experimental results for cases at other values. Nonetheless, the current work would be able to serve as a datum for future research which could incorporate such variables.

5.3. Theoretical considerations

Studies by other researchers concluded that oxide layers tend to develop on the solidifying molten droplets upon ejection [9, 22]. The increase in mass and size of the spatter attributed to oxidation could potentially affect the initial trajectory of the spatter since they could disperse out of the flow at a faster rate downstream. Spatter distribution during the SLM of materials with little or no elements with high affinity to oxidise such as titanium alloy, Ti-6Al-4V could also be investigated on. Despite this, it should be noted that the thickness of the oxide layers are in several as μm reported by Simonelli et al. [9] which is relatively insignificant considering that the spatter size can reach up to 200 μm in diameter.

A more notable contribution for the spatter sizes is the magnitude of recoil pressure present during SLM. Andani et al. [18] was the first to report on the spatter sizes as a result of double laser scanning. It was revealed that when two lasers were in use, spatter diameter ranged from 200 to 720 μm as compared to single laser scanning where the diameter had a range of 120 to 620 mum. With multiple lasers, a greater build up of recoil pressure is generated, producing spatter particles of greater size. In a separate study, Andani et al. [19] also showed that when laser power increased from 250 to 375 W, a greater number of spatter was produced. Wang et al. [12] also showed how laser energy significantly influences spatter generation, where the spattering intensities increased with higher energy. Therefore, future research could involve investigating the effects of laser energy, which includes laser power, speed and also the number of lasers, on the spatter distribution on the powder bed.

On the theoretical side, the transport of spatter by the inert gas flow needs to be modelled mathematically as a multiphase flow while considering the ejection profiles of the spatter from the moving and solidifying melt pool as proper boundary conditions. Fundamental conservation equations for mass, momentum and energy would need to be closed appropriately with the suitable models. The flow conditions whether laminar or turbulent could also play a crucial role in determining the depositing locations of the spatter on the powder bed. Additionally, convection effects which are affected by the temperature of the substrate or the effects of increasing powder layers should also by investigated. Other forces that should be considered are the drag, gravitational and buoyancy forces. Therefore, gas-solid flows in a horizontal configuration could be adopted as suitable models in order to closely replicate the transport phenomena.

6. Conclusion

In this study, three main results have been established. Firstly, the results from the image processing showed a positive linear relationship with the mass which was treated as the ground truth. However, further tests have to be carried out to improve the credibility and suitability of the proposed method as an simple yet efficient in-situ spatter characterisation technique in SLM. Nonetheless, the current image capturing and processing methodology has proven to be able

to serve as an immediate assessment tool to quantify the distribution of mass of spatter on the powder bed.

Secondly, it was shown that the largest spatter in terms of mass and size were observed to be deposited closest to the scanned regions and gradually decreased in the −x direction or downstream of the argon gas flow. Spatter particles were predominantly observed along the scan direction, with minor orthogonal distributions. The increase in gas velocity led to an increase in the transport of heavier and larger spatter, resulting in a more even distribution downstream of the gas flow.

Lastly, the established exponential decay in the Stk number with respect to the distance travelled by the spatter particles, elucidated the limitations in the effectiveness of the inert gas flow in removing the undesired contaminants from the powder bed. As such the reported data for the spatter distribution in SLM of AlSi10Mg could prove to be critical in optimising the gas inlet and outlet designs, in order to successfully eliminate any presence of spatter from the powder bed over larger distances.

Acknowledgements

We would like to thank SLM Solutions Group AG for supporting this project.

References

[1] C. Qiu, C. Panwisawas, M. Ward, H. C. Basoalto, J. W. Brooks, M. M. Attallah, On the role of melt flow into the surface structure and porosity development during selective laser melting, Acta Mater. 96 (2015) 72–79, ISSN 13596454, doi:\bibinfo{doi}{10.1016/j.actamat.2015.06.004}.

[2] S. A. Khairallah, A. T. Anderson, A. Rubenchik, W. E. King, Laser powder-bed fusion additive manufacturing: Physics of complex melt flow and formation mechanisms of pores, spatter, and denudation zones, Acta Mater. 108 (2016) 36 – 45, ISSN 1359-6454, doi:\bibinfo{doi}{http://dx.doi.org/10.1016/j.actamat.2016.02.014}.

[3] S. Ly, A. M. Rubenchik, S. A. Khairallah, G. Guss, M. J. Matthews, Metal vapor micro-jet controls material redistribution in laser powder bed fusion additive manufacturing, Sci. Rep. 7 (1) (2017) 4085, doi:\bibinfo{doi}{DOI:10.1038/s41598-017-04237-z}.

[4] P. Bidare, I. Bitharas, R. Ward, M. Attallah, A. Moore, Fluid and particle dynamics in laser powder bed fusion, Acta Mater. 142 (2017) 107–120, doi:\bibinfo{doi}{https://doi.org/10.1016/j.actamat.2017.09.051}.

[5] D. Low, L. Li, A. Corfe, Effects of assist gas on the physical characteristics of spatter during laser percussion drilling of NIMONIC 263 alloy, Appl. Surf. Sci. 154155 (2000) 689 – 695, ISSN 0169-4332, doi:\bibinfo{doi}{http://dx.doi.org/10.1016/S0169-4332(99)00427-4}.

[6] J. Otegui, H. Kerr, D. Burns, U. Mohaupt, Fatigue crack initiation from defects at weld toes in steel, Int. J. Pres. Ves. Pip. 38 (5) (1989) 385 – 417, ISSN 0308-0161, doi:\bibinfo{doi}{http://dx.doi.org/10.1016/0308-0161(89)90048-3}.

[7] A. C. Popescu, C. Delval, S. Shadman, M. Leparoux, Investigation and in situ removal of spatter generated during laser ablation of aluminium composites, Appl. Surf. Sci. 378 (2016) 102–113, ISSN 01694332, doi:\bibinfo{doi}{10.1016/j.apsusc.2016.03.031}.

[8] N. Read, W. Wang, K. Essa, M. M. Attallah, Selective laser melting of AlSi10Mg alloy: Process optimisation and mechanical properties development, Mater. Des. 65 (2015) 417–424, ISSN 02613069, doi:\bibinfo{doi}{10.1016/j.matdes.2014.09.044}.

[9] M. Simonelli, C. Tuck, N. T. Aboulkhair, I. Maskery, I. Ashcroft, R. D. Wildman, R. Hague, A Study on the Laser Spatter and the Oxidation Reactions During Selective Laser Melting of 316L Stainless Steel, Al-Si10-Mg, and Ti-6Al-4V, Metall. Mater. Trans. A ISSN 1073-5623, doi:\bibinfo{doi}{10.1007/s11661-015-2882-8}.

[10] S. Dadbakhsh, L. Hao, Effect of layer thickness in selective laser melting on microstructure of Al/5 wt.% Fe2O3 powder consolidated parts, Sci. W. J. 2014, doi:\bibinfo{doi}{10.1155/2014/106129}.

[11] Y. Liu, Y. Yang, S. Mai, D. Wang, C. Song, Investigation into spatter behavior during selective laser melting of AISI 316L stainless steel powder, Mater. Des. 87 (2015) 797–806, ISSN 02641275, doi:\bibinfo{doi}{10.1016/j.matdes.2015.08.086}.

[12] D. Wang, S. Wu, F. Fu, S. Mai, Y. Yang, Y. Liu, C. Song, Mechanisms and characteristics of spatter generation in slm processing and its effect on the properties, Mater. Des. 117 (2017) 121–130.

[13] Y. Liu, S. Li, H. Wang, W. Hou, Y. Hao, R. Yang, T. Sercombe, L. C. Zhang, Microstructure, defects and mechanical behavior of beta-type titanium porous structures manufactured by electron beam melting and selective laser melting, Acta Mater. 113 (2016) 56–67, doi:\bibinfo{doi}{https://doi.org/10.1016/j.actamat.2016.04.029}.

[14] C. Yang, Y. Zhao, L. Kang, D. Li, W. Zhang, L. Zhang, High-strength silicon brass manufactured by selective laser melting, Mater. Lett. 210 (2017) 169–172, doi:\bibinfo{doi}{https://doi.org/10.1016/j.matlet.2017.09.011}.

[15] A. Strondl, O. Lyckfeldt, H. Brodin, U. Ackelid, Characterization and control of powder properties for additive manufacturing, JOM 67 (3) (2015) 549–554, doi:\bibinfo{doi}{10.1007/s11837-015-1304-0}.

[16] M. Tang, P. C. Pistorius, Oxides, porosity and fatigue performance of AlSi10Mg parts produced by selective laser melting, Int. J. Fatigue. 94 (2016) 192–201, ISSN 01421123, doi:\bibinfo{doi}{10.1016/j.ijfatigue.2016.06.002}.

[17] A. Ladewig, G. Schlick, M. Fisser, V. Schulze, U. Glatzel, Influence of the shielding gas flow on the removal of process by-products in the selective laser melting process, Addit. Manuf. 10 (2016) 1–9, ISSN 22148604, doi:\bibinfo{doi}{10.1016/j.addma.2016.01.004}.

[18] M. T. Andani, R. Dehghani, M. R. Karamooz-Ravari, R. Mirzaeifar, J. Ni, Spatter formation in selective laser melting process using multi-laser technology, Mater. Des. doi:\bibinfo{doi}{https://doi.org/10.1016/j.matdes.2017.06.040}.

[19] M. T. Andani, R. Dehghani, M. R. Karamooz-Ravari, R. Mirzaeifar, J. Ni, A Study on the Effect of Energy Input on Spatter Particles Creation during Selective Laser Melting Process, Addit. Manuf. doi:\bibinfo{doi}{https://doi.org/10.1016/j.addma.2017.12.009}.

[20] A. Philo, D. Butcher, S. Sillars, C. Sutcliffe, J. Sienz, S. Brown, N. Lavery, A Multiphase CFD Model for the Prediction of Particulate Accumulation in a Laser Powder Bed Fusion Process, in: TMS Annual Meeting & Exhibition, Springer, 65–76, 2018.

[21] A. B. Anwar, Q.-C. Pham, Effect of Unidirectional Scanning with Respect to Gas Flow on Spattered Powder Formation During Selective Laser Melting of AlSi10Mg, Proceedings of the 2nd International Conference on Progress in Additive Manufacturing (Pro-AM 2016) 2 (2016) 531–536.

[22] A. B. Anwar, Q.-C. Pham, Selective laser melting of AlSi10Mg : Effects of scan direction , part placement and inert gas flow velocity on tensile strength, J. Mater. Process. Technol. 240 (2017) 388–396, ISSN 0924-0136, doi:\bibinfo{doi}{10.1016/j.jmatprotec.2016.10.015}.

[23] B. Bidanda, J. Rubinovitz, S. Raman, Development of a spatter index for automated welding inspection using computer vision, Comput. Ind. Eng. 16 (2) (1989) 215–224, doi:\bibinfo{doi}{http://dx.doi.org/10.1016/0360-8352(89)90140-X}.

[24] D. K. Y. Low, L. Li, P. J. Byrd, The effects of process parameters on spatter deposition in laser percussion drilling, Opt. Laser Technol. 32 (5) (2000) 347–354, ISSN 00303992, doi:\bibinfo{doi}{10.1016/S0030-3992(00)00079-7}.

[25] N. Guo, C. Xu, W. Guo, Y. Du, J. Feng, Characterization of spatter in underwater wet welding by X-ray transmission method, Mater. Des. 85 (2015) 156–161, ISSN 0264-1275, doi:\bibinfo{doi}{http://dx.doi.org/10.1016/j.matdes.2015.06.152}.

[26] A. T. Sutton, C. S. Kriewall, M. C. Leu, J. W. Newkirk, A. T. Sutton, C. S. Kriewall, M. C. Leu, J. W. Newkirk, Powder characterisation techniques and effects of powder characteristics on part properties in powder-bed fusion processes, Virtual Phys. Prototyp. 2759 (January), doi:\bibinfo{doi}{10.1080/17452759.2016.1250605}.

[27] J. A. Slotwinski, E. J. Garboczi, P. E. Stutzman, C. F. Ferraris, S. S. Watson, M. A. Peltz, Characterization of metal powders used for additive manufacturing 119 (2014) 460–493, doi:\bibinfo{doi}{10.6028/jres.119.018}.

[28] B. L. Decost, E. A. Holm, Characterizing powder materials using keypoint-based computer vision methods, Comput. Mater. Sci. 126 (2017) 438–445, ISSN 0927-0256, doi:\bibinfo{doi}{10.1016/j.commatsci.2016.08.038}.

[29] G. Repossini, V. Laguzza, M. Grasso, B. M. Colosimo, On the use of spatter signature for in-situ Monitoring of Laser Power Bed Fusion, Addit. Manuf. doi:\bibinfo{doi}{https://doi.org/10.1016/j.addma.2017.05.004}.

[30] A. Realpe, C. Velázquez, Image processing and analysis for determination of concentrations of powder mixtures, Powder Technol. 134 (3) (2003) 193–200, doi:\bibinfo{doi}{https://doi.org/10.1016/S0032-5910(03)00138-4}.

[31] A. Realpe, C. Velázquez, Pattern recognition for characterization of pharmaceutical powders, Powder Technol. 169 (2) (2006) 108–113, doi:\bibinfo{doi}{https://doi.org/10.1016/j.powtec.2006.08.006}.

[32] L. C. Wu, C. Yu, Powder Particle Size Measurement with Digital Image Processing Using Matlab, Adv. Mater. Res. 443-444 (2012) 589–593, doi:\bibinfo{doi}{10.4028/www.scientific.net/AMR.443-444.589}.

[33] J. N. Kapur, P. K. Sahoo, A. K. Wong, A new method for gray-level picture thresholding using the entropy of the histogram, Comput. Vis. Graph Image Process. 29 (3) (1985) 273–285, doi:\bibinfo{doi}{https://doi.org/10.1016/0734-189X(85)90125-2}.

[34] P. Sahoo, C. Wilkins, J. Yeager, Threshold selection using Renyi's entropy, Ptrn. Recognit. 30 (1) (1997) 71–84.

[35] J. Parker, Grey level thresholding in badly illuminated images .

[36] S. Lu, C. L. Tan, Thresholding of badly illuminated document images through photometric correction, in: Proceedings of the 2007 ACM symposium on Document engineering, ACM, 3–8, 2007.

[37] G. Segré, A. Silberberg, Behaviour of macroscopic rigid spheres in Poiseuille flow Part 2. Experimental results and interpretation, J. Fluid Mech. 14 (1) (1962) 136–157.

[38] M. Tirumkudulu, A. Tripathi, A. Acrivos, Particle segregation in monodisperse sheared suspensions, Phys. fluids 11 (3) (1999) 507–509.

[39] D. Kaftori, G. Hetsroni, S. Banerjee, Particle behavior in the turbulent boundary layer. II. Velocity and distribution profiles, Phys. Fluids 7 (5) (1995) 1107–1121.

[40] A. Taniere, B. Oesterle, J. Monnier, On the behaviour of solid particles in a horizontal boundary layer with turbulence and saltation effects, Exp. Fluids 23 (6) (1997) 463–471.

[41] J. K. Eaton, Two-way coupled turbulence simulations of gas-particle flows using point-particle tracking, Int. J. Multiphas. Flow 35 (9) (2009) 792–800.

[42] M. Sommerfeld, J. Kussin, Analysis of collision effects for turbulent gas-particle flow in a horizontal channel. Part II. Integral properties and validation, Int. J. Multiphas. Flow 29 (4) (2003) 701–718.

[43] M. Hussainov, A. Kartushinsky, A. Mulgi, Ü. Rudi, Gas-solid flow with the slip velocity of particles in a horizontal channel, J. Aerosol Sci. 27 (1) (1996) 41–59.

[44] SLM Solutions Machines, URL `https://slm-solutions.com/products/machines`, Accessed: 2018-01-29.